Measuring Seasonal Velocity Variations on an Urban DAS Array

Jihyun Yang and Jeffrey Shragge
Center for Wave Phenomena, Department of Geophysics, Colorado School of Mines, Golden CO 80401
email: jihyunyang@mines.edu

ABSTRACT

Distributed acoustic sensing (DAS) converts a deployed optical fiber into a dense seismic array. Owing to lower maintenance costs, fixed infrastructure, and non-intrusive deployments, DAS-based seismic acquisition provides a cost-effective near-surface monitoring network, especially when using existing telecommunication fiber in urban settings. One interesting application on such networks is applying seismic interferometry, where one can convert the ambient seismic signals into crosscorrelated virtual shot gathers containing subsurface information. We present a case study using a 10-month ambient DAS data set acquired on a fiber array deployed in the metropolitan area of Perth, Australia. We investigate whether long-term seasonal variations can be recovered from ambient urban waveforms on such a DAS array. Weekly stacked interferometric virtual shot gathers reveal bulk 3-4% variations in surface-wave velocities between winter and spring months, which are likely related to variations in near-surface groundwater content. This observation suggests that urban DAS fiber networks may provide an opportunity for urban-subsurface monitoring of groundwater variations.

Key words: Interrogator Design, Coupling, DAS, Velocity, Strain-rate

1 INTRODUCTION

Distributed acoustic sensing (DAS) transforms deployed optical fiber into a distributed seismic sensing network; in particular, as a "large-N" array with dense spatial sampling. Ambient waveform processing can take advantage of the high spatial and temporal sampling rate of large-N DAS arrays. Such acquisition scenarios demonstrably lead to improved tomographic results (Ranasinghe et al., 2018) and more accurate seismic event detection (Li et al., 2018). Additionally, long-term DAS acquisition can be beneficial for a number of monitoring activities including near-surface characterization, environmental studies, and infrastructure monitoring projects (López-Higuera et al., 2011; Dou et al., 2017; Güemes et al., 2018). Many papers have explored near-surface imaging and monitoring DAS applications. Initially, DAS provided a robust system for active-seismic applications such as non-intrusive pipeline and borehole monitoring (Daley et al., 2016; Stajanca et al., 2018). Near-surface passive-seismic applications followed, including permafrost thaw (Ajo-Franklin et al., 2017) and urban-subsurface monitoring (Fang et al., 2020). Zhu et al. (2021) demonstrate the capability of urban DAS array as a multipurpose monitoring system by detecting broadband signals from earthquakes to anthropogenic events.

Our work evaluates whether seasonal variations can be captured using 10 months of ambient DAS recordings acquired on an urban fiber array situated in the central business district (CBD) of Perth, Western Australia. DAS has already shown significant potential for near-surface urban monitoring (Fang et al., 2020; Lindsey et al., 2020) only by using weeks or several months-long data sets. In this work, we aim to capture the dynamics of seasonality in a 10-month time series that covers the fall, winter, and spring in Perth when the hydrological conditions are mostly likely to vary.

We begin by describing the 10-month ambient DAS data set and preprocessing workflows. We then present interferometric cross-correlation results with different stacking durations, an image convergence analysis, and observations of seasonal variations in surface-wave velocity. We conclude by suggesting possible improvements in the ambient processing flow and further applications of urban DAS array for tracking subsurface geophysical variations (e.g., groundwater levels) over calendar time.

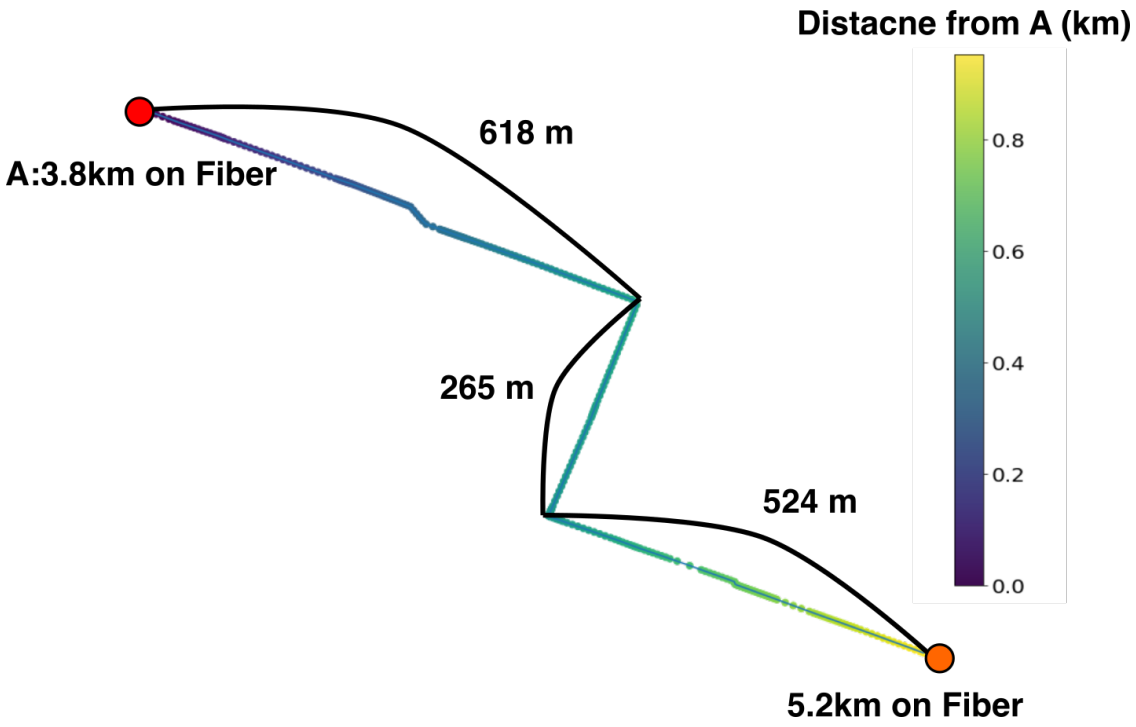

Figure 1. Geometry of the urban Perth CBD DAS array subsection between 3.8-5.2 km pertinent to this discussion.

2 DATASET

Ambient DAS data were acquired on a 7.26 km-long fiber-optic array deployed throughout the Perth CBD. The fiber array and Terra15 Treble interrogator unit (IU) are installed and managed by Terra15 personnel for proprietary purposes. To investigate calendar variations of ambient signals, Terra15 personnel recorded a continuous 150 s-long segment every hour from March 2020 through January 2021. Due to maintenance and other circumstances DAS acquisition occasionally stopped; thus, some variance exists in the daily number of recorded snapshots. A total of 12 TB of HDF5-formatted DAS data were acquired and then bandpass filtered and subsampled to a 72 Hz sampling rate, with a monthly average of 660 recorded segment files, or about 92% of a data set acquired without any disruptions. We obtained relative coordinates of the array subsection relevant for the current investigation (3.8-5.2 km; see Figure 1).

Each file is recorded in deformation-rate or particle-velocity format enabled from the proprietary optical design of Treble IU (Issa et al., 2018). The deformation-rate recording consists of 1484 receivers at a 4.9 m spacing. The data quality degrades after 5.0 km due to optical reflection caused by a connector in the fiber; thus, we only process the data for channels located before this point. Furthermore, to make the ambient signals usable for interferometric analysis, we first transform the DAS velocity data, v, into strain rate by applying a spatial derivative operator along the fiber axis,

$$\dot{\varepsilon_E}(x,t,L_G) \approx \frac{v(x+L_G/2,t)-v(x+L_G/2,t)}{L_G}, \tag{1}$$

where $\dot{\varepsilon_E}$ is the estimated along-fiber strain rate, and L_G is the applied gauge length. For this work, we apply a gauge length of $L_G = 4.9$ m equivalent to the spatial sampling interval.

Figure 2a presents a snapshot of the raw strain-rate DAS recording from July 14th, 2020 at 9AM UTC that exhibits undesirable vertical streaking. This observation motivated us to apply temporal linear trending at each station prior to strain-rate calculation, which effectively eliminates the unwanted DC component offset. Figure 2b shows a strain-rate data snapshot after linear detrending, which has helped to balance the overall section.

Figure 3 presents an 18-day spectrogram from April 2020 for the detrended data at a point located at 4.2 km distance along the array. We observe peak energy between 23-27 Hz and to a lesser extent between 12-16 Hz; energy is also stronger overall during the daytime, which is expected due to increased anthropogenic activities during these time periods.

3 INTERFEROMETRIC PROCESSING

We follow the general ambient interferometric data processing workflow presented in Bensen et al. (2007), the first step of which consists of partitioning the data volume into short segment windows (here 150 s). The windowed random ambient signals are transformed into virtual shot gathers (VSGs) using seismic interferometry (Snieder, 2004; Wapenaar et al., 2010). For reasons of computational efficiency, we perform cross-correlation in the frequency domain. We first apply a Fourier transform of the nth strain-rate DAS event window, $u_n(x_i, t)$, to generate frequency-domain response $u_n(x_i, \omega)$, where t is time, x_i represents either the location of the virtual source x_A or the virtual receiver x_B, and ω is angular frequency. We then compute the cross-correlation and stack over all windows before computing the inverse Fourier transform. Thus, we create a VSG volume G_{XC} according to

$$G_{XC}(x_A, x_B, \tau) = \mathcal{F}^{-1}\left[\sum_{n=1}^{N} u_n(x_A, \omega)\overline{u_n(x_B, \omega)}\right], \tag{2}$$

where $\mathcal{F}^{-1}$ is the inverse Fourier transform operator, n is the event window index, N is the total number of event windows, $\overline{u}$ indicates complex conjugate of wavefield u, and τ represents the two-sided temporal correlation lag.

3.1 Image Convergence

The purpose of applying a stacking process is to enhance the signal-to-noise ratio (SNR) of the VSGs. Ideally, stacking for infinite time duration would achieve convergence. In this work, we compare the data stacking result with a simple convergence model (Issa et al., 2017) that predicts the convergence in terms of the image variance of the cross-correlation images. This calculation is given by

$$I(d, \tau) = I_{static}(d) + \frac{1}{\tau}\int_0^{\tau} N(d, \tau')d\tau', \tag{3}$$

where $I_{static}(d)$ is a static image that is equivalent to the converged image after stacking a "sufficient" number of windows, d is correlation lag, and τ' is a temporal integration variable.

Taking variance of the both site of equation 3 results in

$$I_{var}(\tau) = Var_d(I_{static}(d)) + \frac{1}{\tau^2}Var_d\left(\int_0^{\tau} N(d, \tau')\right)d\tau' = Var_d(I(d, \tau)). \tag{4}$$

The noise variance can be expanded into sum of its subintervals with the average written as:

$$\frac{1}{\Delta\tau^2}Var_d\left(\int_0^{\tau} N(d, \tau')\right)d\tau' = \sum_{n=1}^{N} Var_d\left(\frac{1}{\Delta\tau}\int_{(n-1)\Delta\tau}^{n\Delta\tau} N(d, \tau')\right) = \sum_{n=1}^{N} N_{var}(n). \tag{5}$$

Defining

$$\overline{N}_{var} = \frac{1}{N}\sum_{n=1}^{N} N_{var}(n) \tag{6}$$

reduces the image converge model to:

$$I_{var}(\tau) = Var_d(I_{static}(d)) + \frac{\Delta\tau}{\tau}\overline{N}_{var}, \tag{7}$$

which indicates that the convergence rate of the VSGs image variance and the stacking time are inversely proportional.

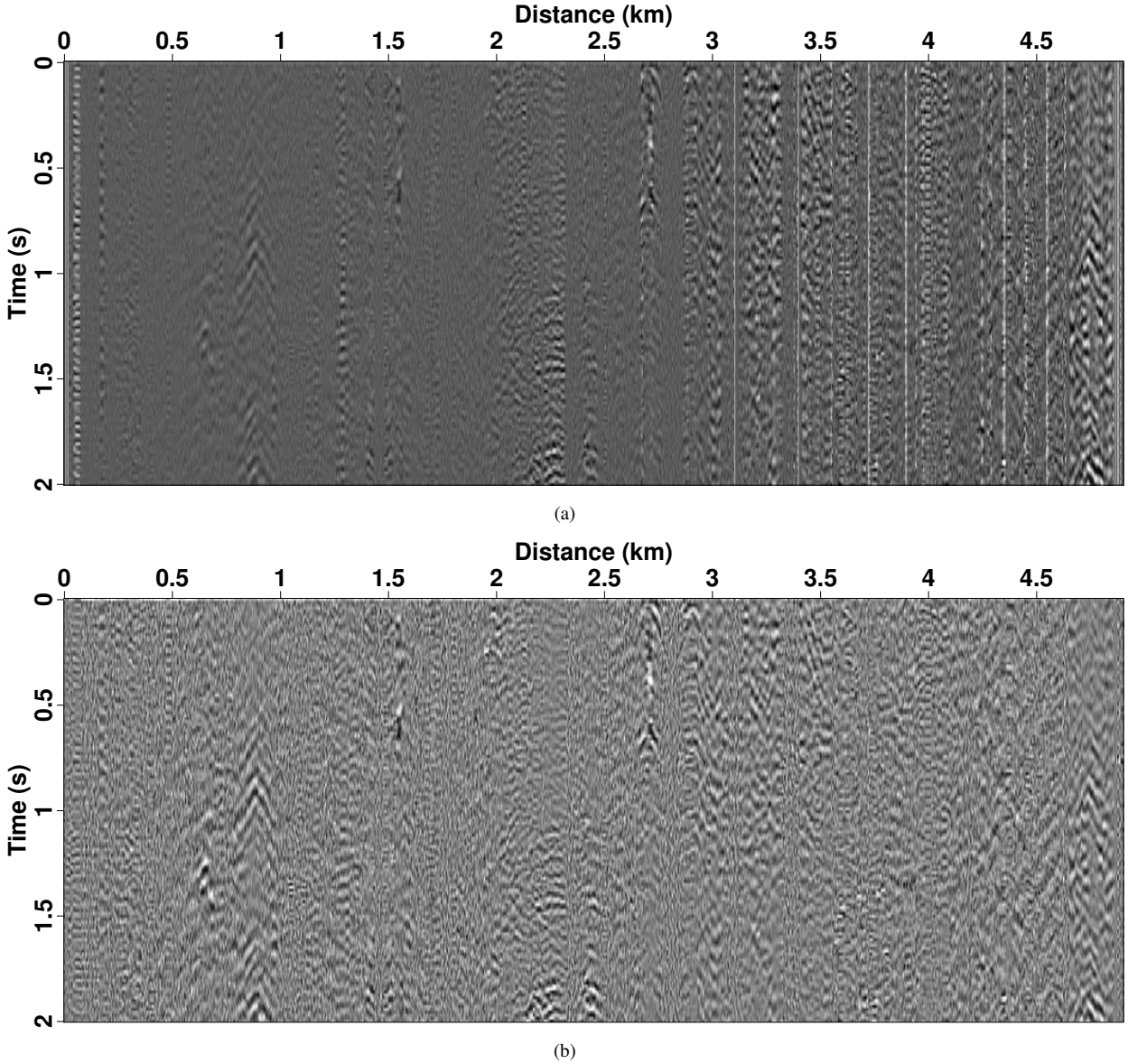

Figure 2. Representative 2.0 s strain-rate panel recorded at 9AM UTC July 14th, 2020 (a) before and (b) after applying detrending processing.

4 RESULTS

We stacked the 150 s windows cross-correlated data to enhance the SNR of the virtual shot and observe the convergence of the image variance of the interferometric cross-correlation analysis. We fit the convergence model (equation 7) to the convergence curve from the data set. We note that image variance calculation achieved convergence after stacking roughly 50 files, representing just over two days of hourly 2.5 minute recordings. The convergence of the image variance calculation is observed in both the actual and modeled convergence curves (Figure 4a) as well as the image variance gradient plot (Figure 4b).

4.1 Time-lapse observations

Figure 5 shows weekly stack VSGs using a master trace located at 4.61 km on the fiber for four different dates separated by a minimum of two months. The vertical black lines indicate the points where the fiber array bends in a 90° angle (i.e., at 4.41 km and 4.68 km on the array, see Figure 1). Generally, the average apparent moveout velocity (∼0.22 km/s) of (presumably) Rayleigh

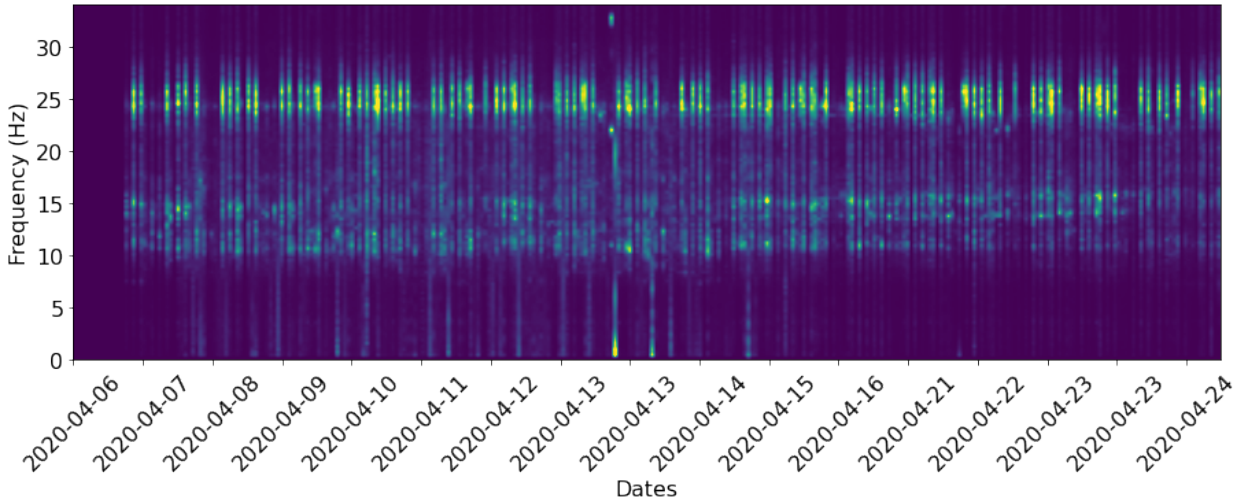

Figure 3. An 18-day spectrogram from April 2020 extracted from the fiber location at 4.2 km.

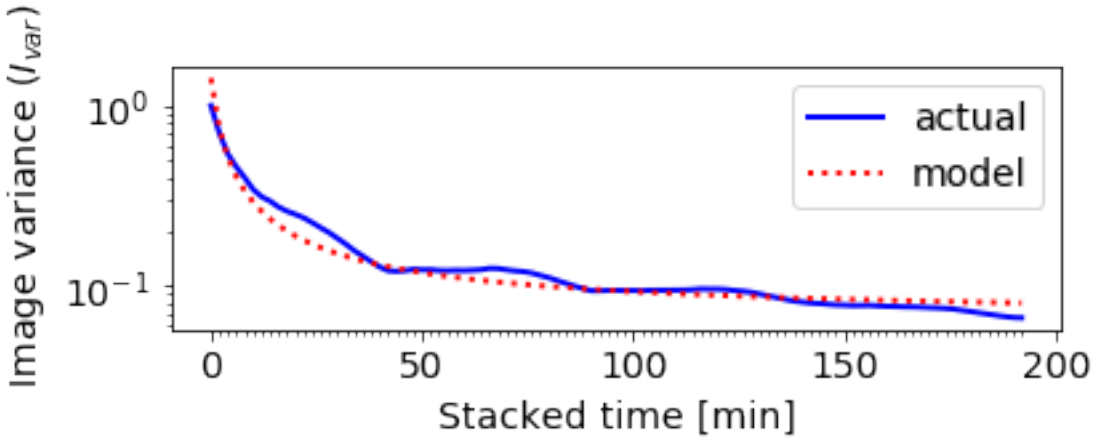

(a)

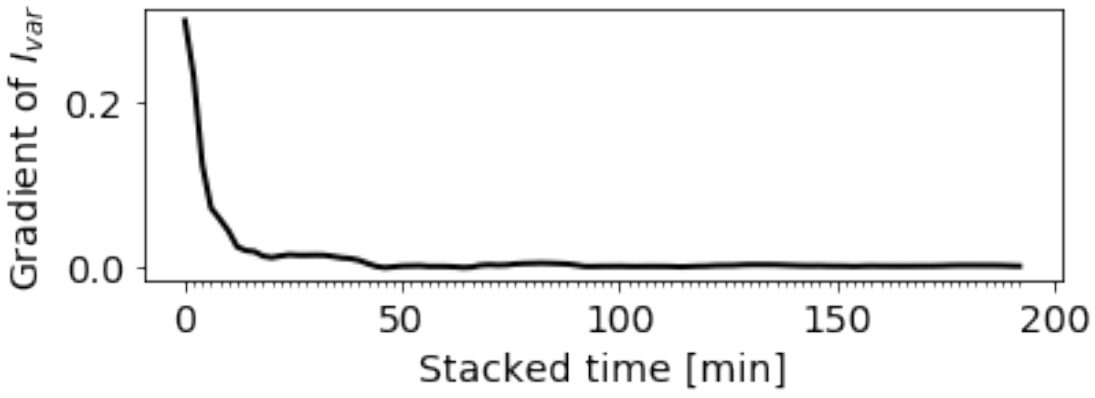

(b)

Figure 4. (a) Image variance convergence curve calculated from VSG stacking for the DAS data (solid blue curve) and the theoretical convergence model (dotted red curve). (b) VSG data image variance convergence gradient.

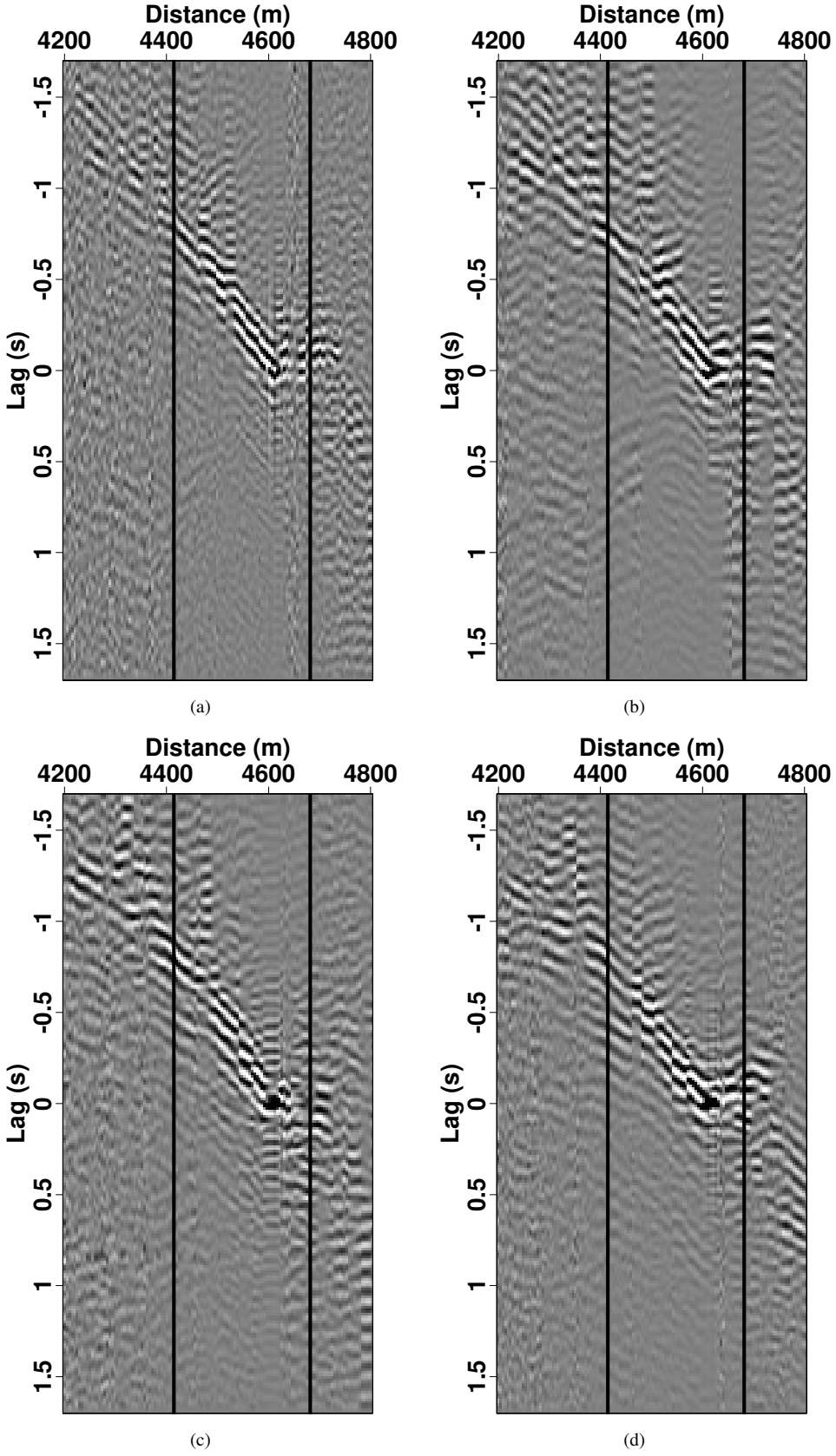

Figure 5. Weekly VSG stacks on different dates: (a) 1 April 2020, (b) 12 June 2020, (c) 5 August 2020, and (d) 4 January 2021. The vertical black lines indicate where fiber array bend 90° (i.e., at 4.41 km and 4.68 km; see Figure 1.)

waves is consistent with near-surface geologic materials that are expected to be Quaternary Swan River deposits (Davey, 2018). The four example panels show moderate time-varying wavefield behavior in terms of observed amplitudes and observed apparent velocities.

To investigate the time-varying behavior in detail, we concatenate 43 weekly stack VSGs and extract the same trace at a fixed source-receiver offset to generate time-lapse 2-D panels. Figure 6a and 6b shows two such panels from different fixed source-receiver offsets of 0.21 km and 0.18 km. There are clear traveltime shifts are evident in two panels showing the curvature of the same selected (presumably) Rayleigh-wave arrival phase. On Week 11 (the first week of June 2020), we observe discontinuities over various offsets. This may have been caused by extreme weather events in Perth, such as winter heavy storms and rainfall commonly observed in Perth when June and July are peak months of storm activity. We calculate the traveltime variation of different fixed offset panels from the latest and earliest arrivals of the single waveform (respectively blue and red dots; see Figure 6a and 6b). The mean travel-time variation averaged over six fixed source-receiver offsets is 3.2%. Figure 6c and 6d shows different 2-D panels extracted at two fixed time lags (-0.65 s and -0.85 s). We again note the previously observed curvature and Week 11 discontinuity.

4.2 Surface-wave Dispersion Analysis

We perform multichannel analysis of surface waves (MASW) on week-stacked gathers to extract the phase-velocity spectra. Figure 7 displays the varying phase-velocity spectra from the week of March 31th, May 4th, June 8th, and July 27th, 2020. Significant energy in the 7-10 Hz frequency band has a consistent phase velocity of around 0.3 km/s. During the heavy rainfall season (June to August) in Perth corresponding to the dispersion panels in Figure 7c and 7d, strong energy is observed around 10 Hz, which we suspect to be associated with a higher mode. We compute the average spectra which represents the monthly varying dispersion panels of April, July, September and December 2020 (See Figure **??**).

The shear-wave velocity in the top 30 m (VS_{30}) is a useful proxy for short-period ground motion prediction (Code, 2005; Kanlı et al., 2006). We obtain the shear-wave velocity in the top 30 m (VS_{30}) by inverting the dispersion picks (e.g., those shown in Figure 9a). We use particle swarm optimization (PSO) (Poli et al., 2007), one of the global optimization schemes. The parameter bounds of S-wave velocity are 0.001 km/s and 3.0 km/s for the lower and upper bounds, respectively. The resulting model shows varying VS_{30} on each week-stacking period.

The estimated overall velocity variation of 5.8% is comparable with the traveltime variance observed in Figure 6a and 6b. We observe the velocity decrease during the winter rainy period (June-August) and increase during the onset of spring (Figure 9b), following the relationship between S-wave velocity and water content. Miao et al. (2018) report a near-surface S-wave velocity decrease of 1-3% for low-intensity rain events, and up to a 10% velocity decrease after heavy rainfalls in Northeast Honshu, Japan. They summarize the effects of rainfall on near-surface S-wave velocity in regard to the threshold; in short, only rainfall events exceeding this threshold affect the near-surface S-wave velocity profile. According to the Perth Metro rainfall record, Perth Metro rainfall falls in the heavy-rainfall class and consequently, we observe 3.2% traveltime and 5.8% VS_{30} variation.

5 FURTHER PROCESSING

While we successfully observed the seasonal near-surface S-wave velocity variation from the 10-month ambient DAS recording through the data preprocessing and interferometric analysis outlined above, an urban data set with persistent noise sources might be demanding for conventional workflows. To achieve more robust characteristics from this specific data set, we applied a tailored workflow involving selective stacking and debursting processing schemes and compare the result with former results.

5.1 Selective stacking

Ideally, a longer duration of stacking time results in an improvement of signal quality in VSGs or empirical Green's function. However, as shown in Figure 4, the image variance reaches its convergence at 50 minutes of stacking, equivalent to 2.5 weeks of the dataset. Xie et al. (2020) improve VSG stacking by selecting only the gathers that increase the RMS ratio after their addition into the stack. This work indicates RMS works as a useful indicator to accept/reject the window. Here, we use the RMS value of a subset of data denoted as the orange and yellow boxes in Figure 10. We consider the orange (I_N) and yellow (I_S) boxes as a representative samples of noise and signal, respectively. We choose data windows having RMS ratios ($I_{S_{rms}}/I_{N_{rms}}$) above the threshold value. A threshold can be set up accordingly to the RMS distribution.

For this work, we set up the threshold as 1.1 and thereby reject 60% of the dataset. Overall, 76% of day-stacking panels show

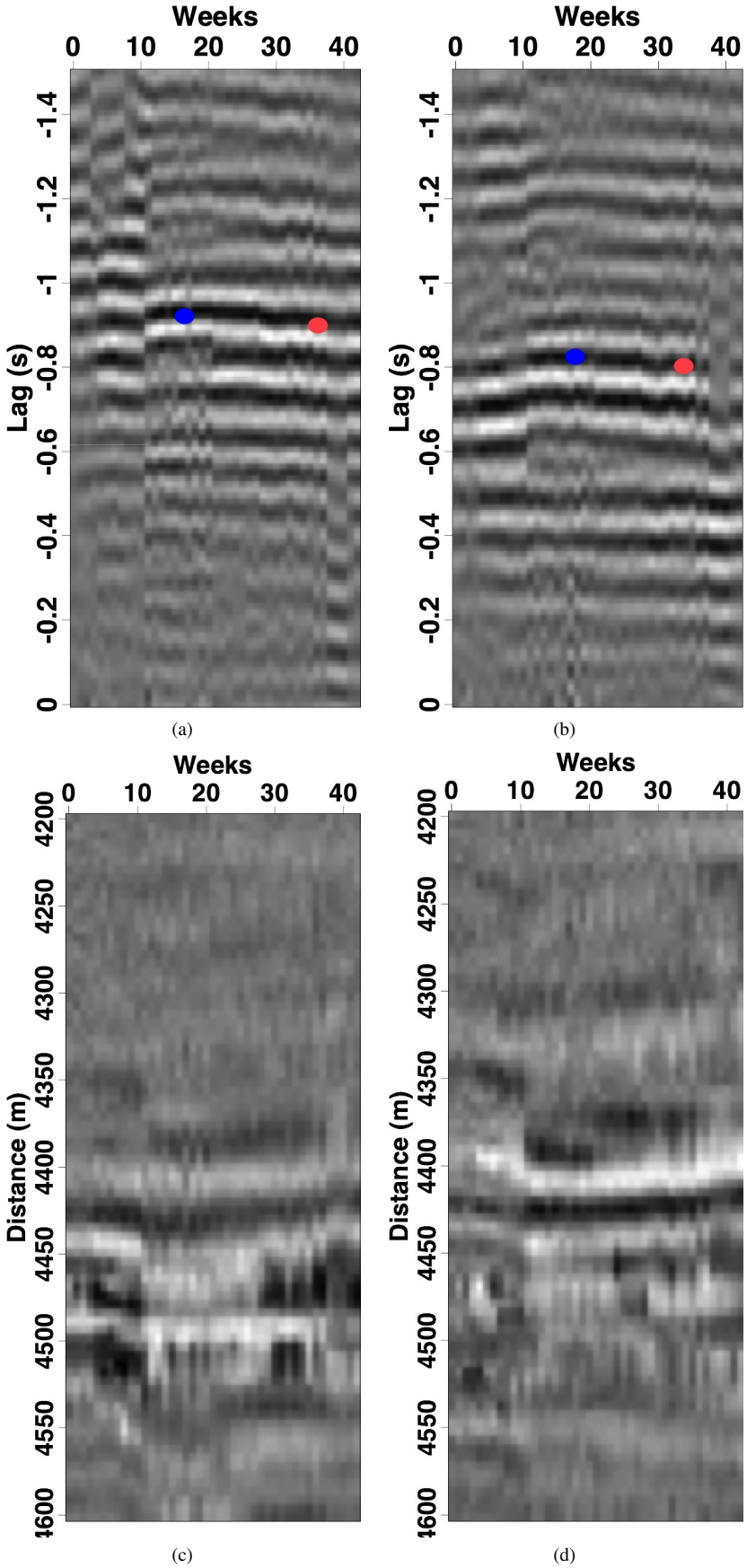

Figure 6. Calendar time-lapse behavior over a 43-week period. 2-D lag-week panel extracted at (a) 0.21 km and (b) 0.18 km fixed source-receiver offsets. The blue and red dots are examples of picked arrival times for the latest and earliest arrivals of a consistent Rayleigh-wave arrival. The mean traveltime variation calculated over six different offsets is 3.2%. 2-D offset-week panels extracted at (c) -0.65 s and (d) -0.85 s correlation lag.

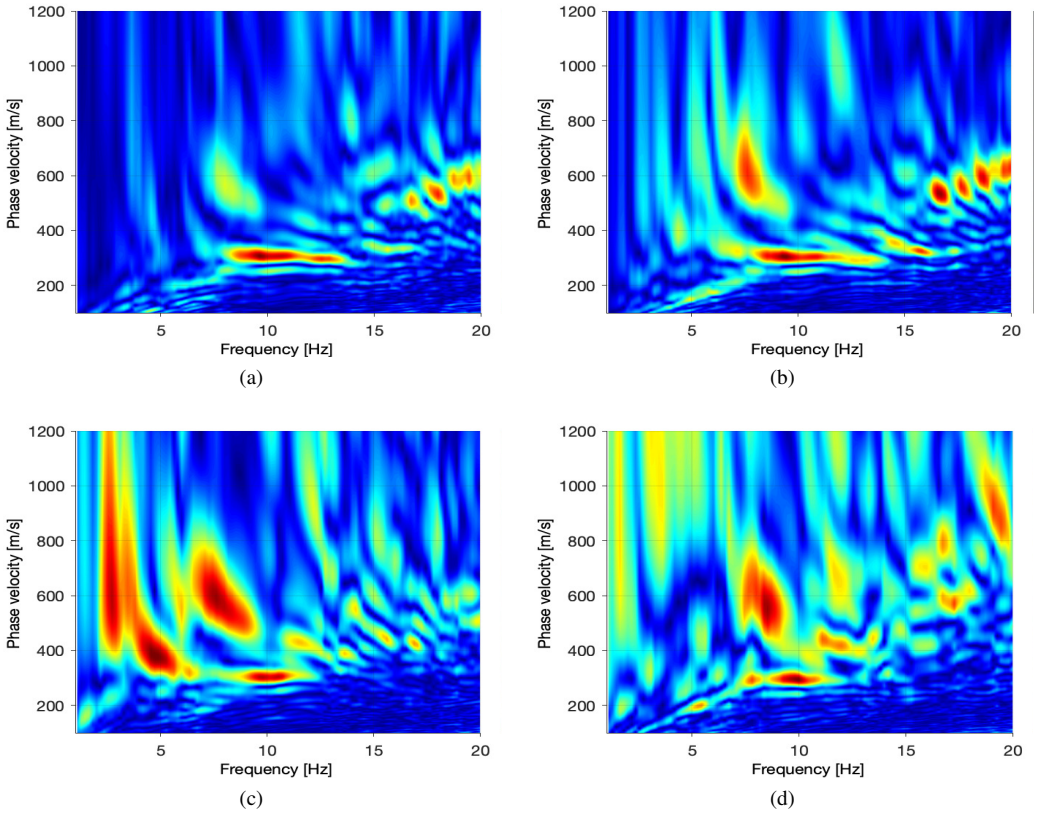

Figure 7. Dispersion analysis of week-stacked data at (a) March 31th, 2020 (b) May 4th, 2020 (c) June 8th, 2020 (d) July 27th, 2020

increase in RMS value, which is apparent in day-stacking result on April 9th, 2020 with and without selective stacking (see Figure 11). It is clear that noise located near zero lag (Figure 11a) is removed in selective stack (Figure 11b).

5.2 Debursting

The narrow-band ringing energy is present in many panels, as is illustrated in week-stack results (Figure 7). We apply time and frequency debursting to improve convergence by removing sudden temporal bursts or spurious frequencies. The debursting operation involves the L_1 IRLS debursting approach of (Claerbout, 2014) and the modified frequency-domain debursting discussed in (Girard and Shragge, 2020). As demonstrated in spectra of the dataset before and after debursting (Figure 12), we expect better balancing in frequency amplitude after the debursting procedure and thus effective elimination of the ringing events, as is shown by the pre- and post-debursting example shown in Figure 13a and 13b, respectively.

6 DISCUSSION

Dispersion analysis is a useful tool for extracting phase information and the associated S-wave velocity profile. We are currently working on retrieving relative coordinates of the array for further processing. Cross-correlation stacking results converge around 50 segments, equivalent to just over two days of hourly 2.5-min window stacking. We suspect the resulting curve (Figure 4) achieves early convergence due to the absence of strong non-repeatable noise in the cross-correlation panels. Further stacking improvements likely are possible with enhanced stacking methods. Selective stacking method based on the RMS ratio of signal and noise windows (Xie et al., 2020) and machine learning-based clustering technique (Viens and Iwata, 2020) could be used to eliminate windows that adversely contribute to the RMS of coherent VSGs.

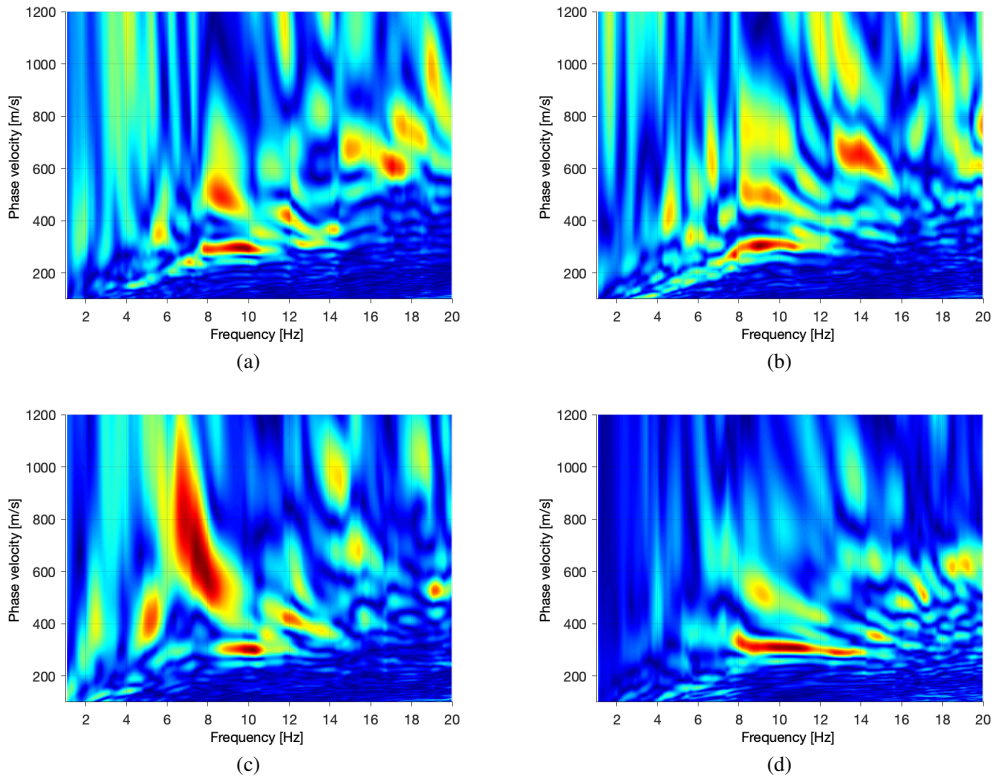

Figure 8. Dispersion analysis of month-stack data for (a) April, (b) July, (c) October and (d) December 2020.

7 CONCLUSIONS AND FUTURE WORK

We present a case study that investigates the seasonal changes observed in a 10-month ambient DAS dataset recorded from fiber located in the urban center of Perth, WA. The interferometric analysis resulted in VSGs that exhibit travel-time variations in observed wavefield arrivals over the 43-week recording period, with an interpreted 3.2% maximum calendar change in the observed Rayleigh-wave velocities. Future work will investigate inverting more optimized VSGs for subsurface properties and examining noted correlations with environmental factors (e.g., water-table changes).

8 ACKNOWLEDGEMENTS

We thank the Center for Wave Phenomena (CWP) sponsors, whose support made this research possible. We also would like to thank A. Noetzli, N. Issa and M. Roelens (Terra15) for providing the dat aset and useful technical suggestions. The reproducible numerical examples and plots in this paper use the Madagascar software package (www.ahay.org).

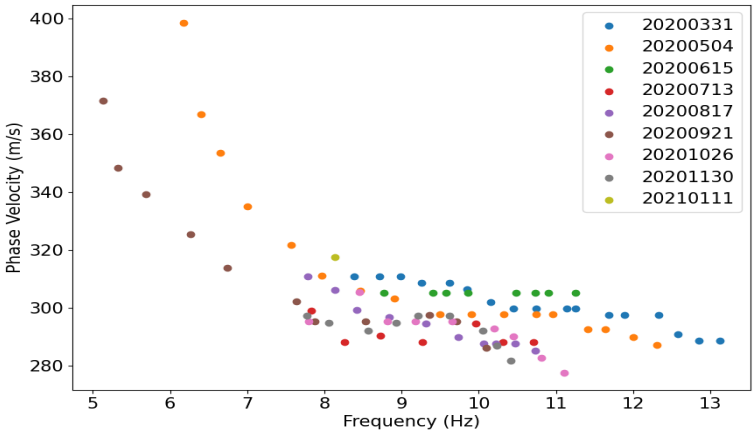

(a)

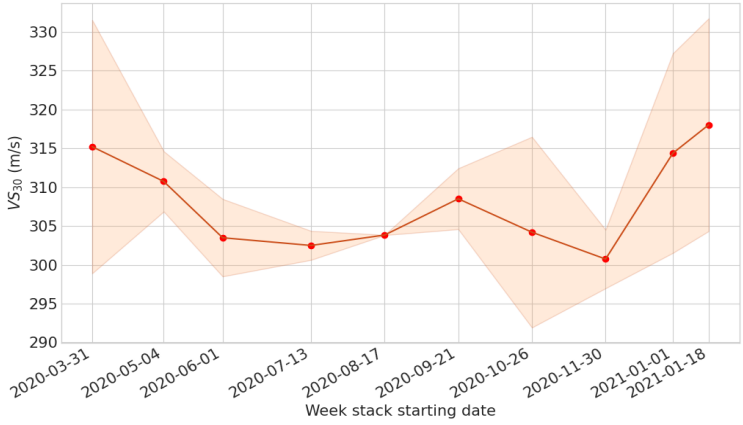

(b)

Figure 9. (a) Fundamental mode pickings from weekly phase velocity-frequency spectra. (b) Inverted VS_{30} using the picks shown in (a).

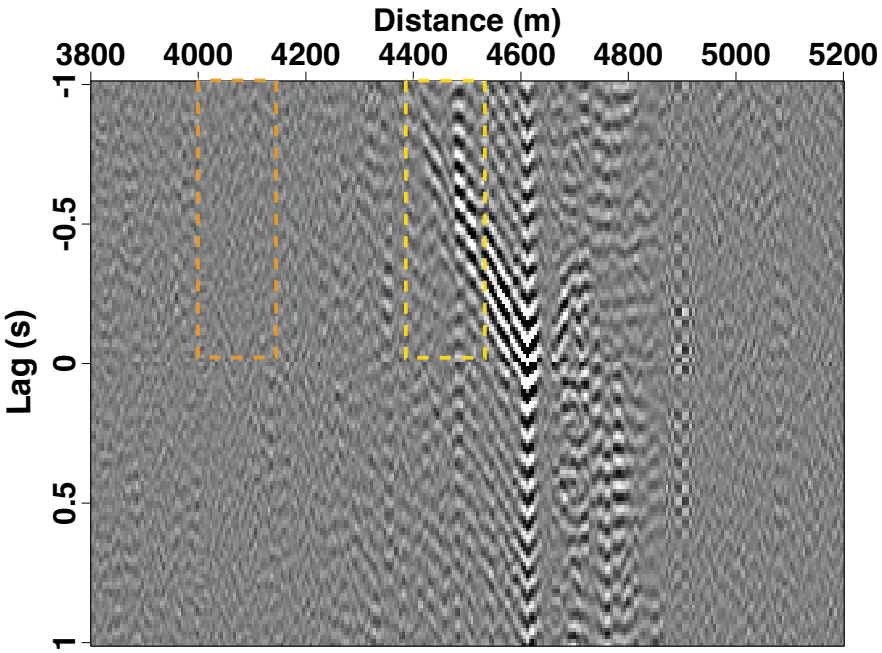

Figure 10. The orange (I_N) and yellow (I_S) boxes are representative estimates of noise and signal, respectively. The RMS ratio between two selected windows can be used as select/rejecting criterion for selective stacking.

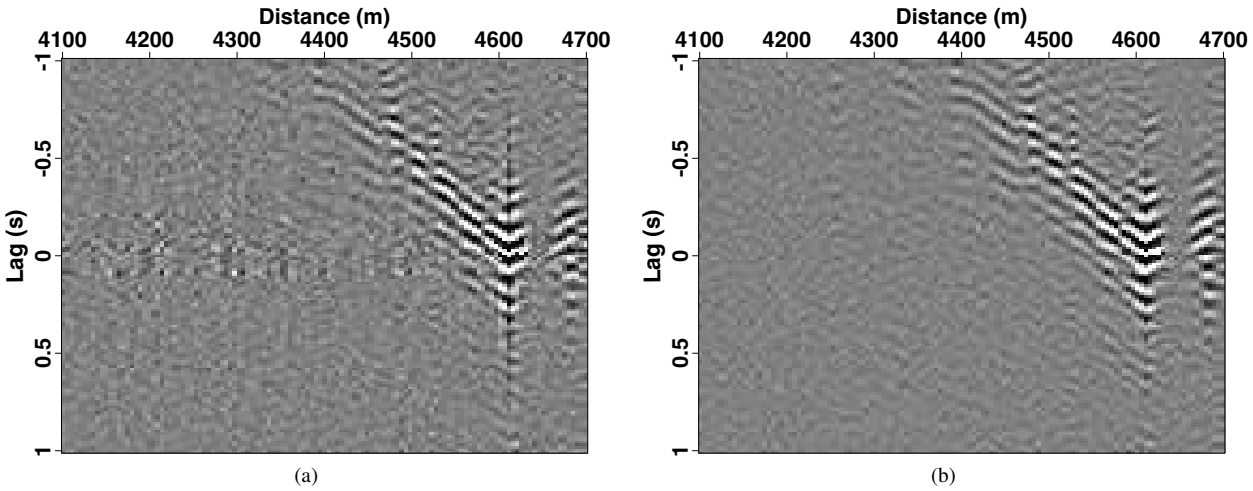

Figure 11. Day-stack results on April 9th, 2020. (a) The result of stacking entire daily data set. (b) The result of stacking of selected windows with RMS ratio above the threshold.

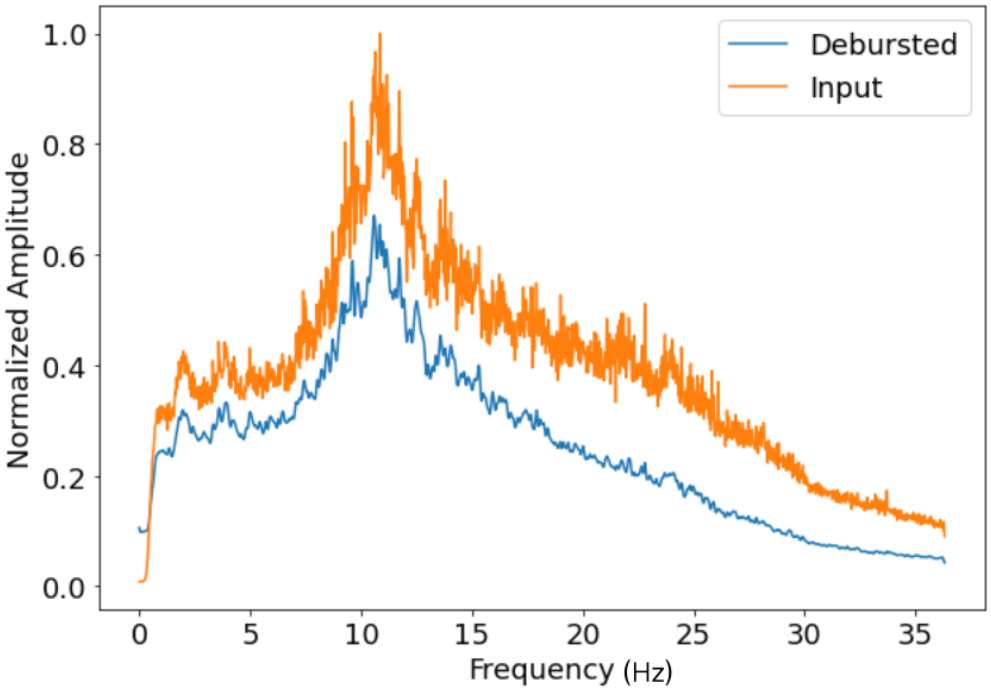

Figure 12. Frequency spectra of the data set before and after debursting. Debursted data (blue curve) shows a gradual drop near 0 Hz compared to that of input (orange curve) and overall better balance in the frequency band.

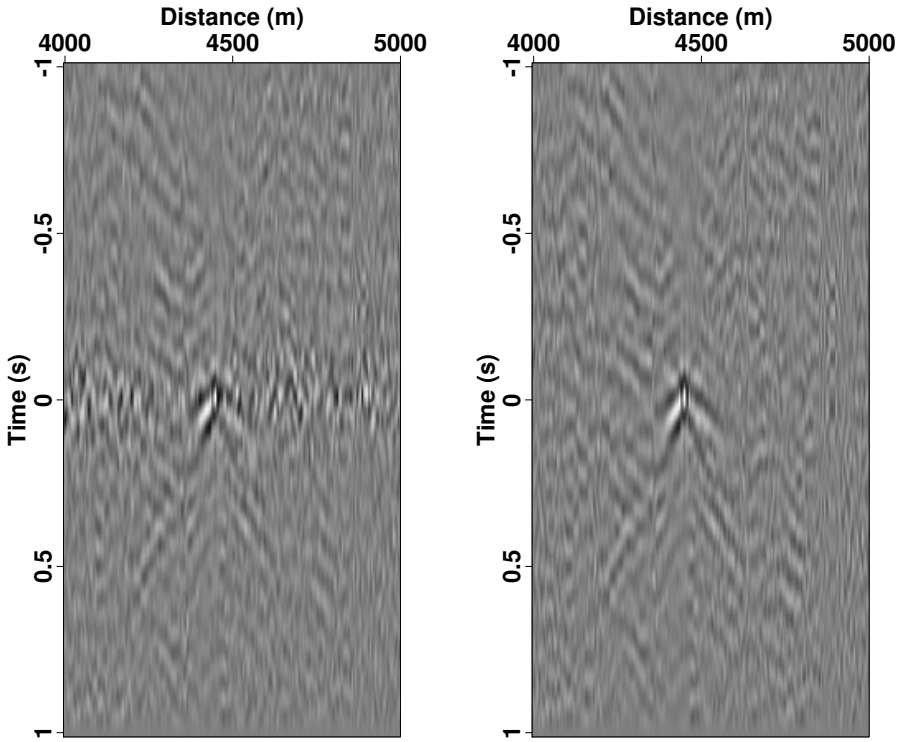

(a) (b)

Figure 13. Day-stacking result on August 2th, 2020 showing the VSG (a) before and (b) after applying the debursting workflow. Spikes around zero-lag on (a) are removed through the debursting process.

REFERENCES

Ajo-Franklin, J., S. Dou, T. Daley, B. Freifeld, M. Robertson, C. Ulrich, T. Wood, I. Eckblaw, N. Lindsey, E. Martin, et al., 2017, Time-lapse surface wave monitoring of permafrost thaw using distributed acoustic sensing and a permanent automated seismic source, *in* SEG Technical Program Expanded Abstracts 2017: Society of Exploration Geophysicists, 5223–5227.

Bensen, G., M. Ritzwoller, M. Barmin, A. L. Levshin, F. Lin, M. Moschetti, N. Shapiro, and Y. Yang, 2007, Processing seismic ambient noise data to obtain reliable broad-band surface wave dispersion measurements: Geophysical journal international, **169**, 1239–1260.

Claerbout, J., 2014, Geophysical image estimation by example: Lulu. com.

Code, P., 2005, Eurocode 8: Design of structures for earthquake resistance-part 1: general rules, seismic actions and rules for buildings: Brussels: European Committee for Standardization.

Daley, T., D. Miller, K. Dodds, P. Cook, and B. Freifeld, 2016, Field testing of modular borehole monitoring with simultaneous distributed acoustic sensing and geophone vertical seismic profiles at citronelle, alabama: Geophysical Prospecting, **64**, 1318–1334.

Davey, N., 2018, Bore completion report for the kings park formation groundwater investigation: Department of Water and Environmental Regulation, Hydrogeological Record Series, HR 397.

Dou, S., N. Lindsey, A. M. Wagner, T. M. Daley, B. Freifeld, M. Robertson, J. Peterson, C. Ulrich, E. R. Martin, and J. B. Ajo-Franklin, 2017, Distributed acoustic sensing for seismic monitoring of the near surface: A traffic-noise interferometry case study: Scientific reports, **7**, 1–12.

Fang, G., Y. E. Li, Y. Zhao, and E. R. Martin, 2020, Urban near-surface seismic monitoring using distributed acoustic sensing: Geophysical Research Letters, **47**, e2019GL086115.

Girard, A. J., and J. Shragge, 2020, Automated processing strategies for ambient seismic data: Geophysical Prospecting, **68**, 293–312.

Güemes, A., A. Fernández-López, P. F. Díaz-Maroto, A. Lozano, and J. Sierra-Perez, 2018, Structural health monitoring in composite structures by fiber-optic sensors: Sensors, **18**, 1094.

Issa, N., M. Roelens, and S. Frisken, 2018, Distributed optical sensing systems and methods: PCT Patent Application PCT/AU2018/050775.

Issa, N. A., D. Lumley, and R. Pevzner, 2017, Passive seismic imaging at reservoir depths using ambient seismic noise recorded at the otway co2 geological storage research facility: Geophysical Journal International, **209**, 1622–1628.

Kanlı, A. I., P. Tildy, Z. Prónay, A. Pınar, and L. Hermann, 2006, Vs 30 mapping and soil classification for seismic site effect evaluation in dinar region, sw turkey: Geophysical Journal International, **165**, 223–235.

Li, Z., Z. Peng, D. Hollis, L. Zhu, and J. McClellan, 2018, High-resolution seismic event detection using local similarity for large-n arrays: Scientific reports, **8**, 1–10.

Lindsey, N. J., S. Yuan, A. Lellouch, L. Gualtieri, T. Lecocq, and B. Biondi, 2020, City-scale dark fiber das measurements of infrastructure use during the covid-19 pandemic: Geophysical research letters, **47**, e2020GL089931.

López-Higuera, J. M., L. R. Cobo, A. Q. Incera, and A. Cobo, 2011, Fiber optic sensors in structural health monitoring: Journal of lightwave technology, **29**, 587–608.

Miao, Y., Y. Shi, and S.-Y. Wang, 2018, Temporal change of near-surface shear wave velocity associated with rainfall in northeast honshu, japan: Earth, Planets and Space, **70**, 1–11.

Poli, R., J. Kennedy, and T. Blackwell, 2007, Particle swarm optimization: Swarm intelligence, **1**, 33–57.

Ranasinghe, N., L. Worthington, C. Jiang, B. Schmandt, T. Finlay, S. Bilek, and R. Aster, 2018, Upper-crustal shear-wave velocity structure of the south-central rio grande rift above the socorro magma body imaged with ambient noise by the large-n sevilleta seismic array: Seismological Research Letters, **89**, 1708–1719.

Snieder, R., 2004, Extracting the Green's function from the correlation of coda waves: A derivation based on stationary phase: Physical Review E, **69**, 046610.

Stajanca, P., S. Chruscicki, T. Homann, S. Seifert, D. Schmidt, and A. Habib, 2018, Detection of leak-induced pipeline vibrations using fiber—optic distributed acoustic sensing: Sensors, **18**, 2841.

Viens, L., and T. Iwata, 2020, Improving the retrieval of offshore-onshore correlation functions with machine learning: Journal of Geophysical Research: Solid Earth, **125**, e2020JB019730.

Wapenaar, K., D. Draganov, R. Snieder, X. Campman, and A. Verdel, 2010, Tutorial on seismic interferometry: Part 1—basic principles and applications: Geophysics, **75**, 75A195–75A209.

Xie, J., Y. Yang, and Y. Luo, 2020, Improving cross-correlations of ambient noise using an rms-ratio selection stacking method: Geophysical Journal International, **222**, 989–1002.

Zhu, T., J. Shen, and E. R. Martin, 2021, Sensing earth and environment dynamics by telecommunication fiber-optic sensors: an urban experiment in pennsylvania, usa: Solid Earth, **12**, 219–235.